J Clust Sci (2016) 27:965–978
DOI 10.1007/s10876-015-0963-x

ORIGINAL PAPER

Synthesis and Evaluation of Microstructural and Magnetic Properties of Cr^{3+} Substitution Barium Hexaferrite Nanoparticles ($BaFe_{10.5-x}Al_{1.5}Cr_xO_{19}$)

Akbar Hojjati Najafabadi[1] · Ali Ghasemi[1] · Reza Mozaffarinia[1]

Received: 26 September 2015 / Published online: 6 January 2016

Abstract Pure barium ferrite and $BaFe_{10.5-x}Al_{1.5}Cr_xO_{19}$ (x = 0, 0.5, 1.0, 1.5, 2.0) nanoparticles were synthesized by auto-combustion sol–gel method. The effect of substituting Fe^{3+} ions by Al^{3+} and Cr^{3+} ions on the structural, chemical composition, morphology and magnetic properties of $BaFe_{12}O_{19}$ and $BaFe_{10.5-x}Al_{1.5}Cr_xO_{19}$ hexaferrites have been investigated using X-ray diffraction, Fourier transform infrared spectroscopy, field emission scanning electron microscopy and vibrating sample magnetometer (VSM), respectively. The results confirmed that the hexagonal phase has been formed in all of nanoparticles and the value of lattice parameter (c) decreased, while the value of lattice parameter (a) remained nearly constant with the increase in Cr^{3+} ions contents in comparison to pure barium ferrite. The crystallite size and mean particle size of the nanoparticles lie in the ranges 33–42 and 35–70 nm, respectively. The VSM measurements show that with substituting Al and Cr cations in the hexagonal structure of barium ferrite, the saturation magnetization (M_s) and remanence magnetization (M_r) of the nanoparticles reduce, while coercive field (H_c) increased from 4.45 kOe for pure barium ferrite to 6.9 kOe for $BaFe_{10.5}Al_{1.5}O_{19}$ (x = 0) due to the increase in the magnetocrystalline anisotropy and the decrease of the particle size.

Keywords Hexaferrite · Cr-substituted · Structural characterization · Magnetic properties

✉ Akbar Hojjati Najafabadi
a_hojjati@yahoo.com

[1] Department of Materials Engineering, Malek Ashtar University of Technology, Shahin Shahr, Isfahan, Iran

Introduction

The M-type hexagonal hard ferrites $BaFe_{12}O_{19}$ with magnetoplumbite structure have been discovered in the 1950s and they have many interest for low costs and their specific magnetic properties like high coercive field, their high magnetization, high Curie temperature, excellent chemical stability, mechanical strength and corrosion resistivity [1–3]. Due to their properties, these ferrites have many applications such as data storage and recording, permanent magnets, electrical and microwave devices, plastoferrites, RAM and microwave/EM wave absorption, magnetoelectric (ME) and multiferroic (MF) applications and chip inductors [1, 2].

As it is well known that the magnetic properties can be changed by substitution for the Fe^{3+} with divalent, trivalent and tetravalent ions in crystallographic sites which are three octahedral (2a, $4f_2$ and 12k), one trigonal bipyramidal (2b) and one tetrahedral ($4f_1$) [4–6]. One of the most important of magnetic properties for achievement to above mentioned applications is coercive field (H_c). The coercive field can be remarkably changed with changing of magnetocrystalline anisotropy field and superexchange interaction [4, 5, 7–9]. When trivalent ions (like Al^{3+} and Cr^{3+}) are entered to the lattice of $BaFe_{12}O_{19}$, the coercive field could be increased due to the substitution of these ions instead of Fe^{3+} ions by effect on magnetocrystalline anisotropy field and superexchange interaction. On the other hand, with substituting Al^{3+} and Cr^{3+} ions in crystal structure of barium ferrite, it can be reduced particles size and lead to increase of the coercive field [10–12].

In the current study, the $BaFe_{10.5-x}Al_{1.5}Cr_xO_{19}$ (x = 0, 0.5, 1.0, 1.5, 2.0) nanoparticle were synthesized via auto-combustion sol–gel method. Then, the structural characteristics and magnetic properties of substituted barium ferrite were investigated and discussed. The substituted hexagonal nanoparticles have been characterized using the X-ray diffraction (XRD), Fourier transform infrared spectroscopy (FTIR) and field emission scanning electron microscopy (FE-SEM). The vibrating sample magnetometer (VSM) were also used to investigate the effect of Al^{3+} and Cr^{3+} ions substitution contents on magnetic properties of barium ferrite.

Materials and Methods

Preparation of Nanoparticles

The raw materials used in the present work were purchased from Merck and were used as received. The pure barium hexaferrite and $BaFe_{10.5-x}Al_{1.5}Cr_xO_{19}$ nanoparticles with different composition (x = 0, 0.5, 1.0, 1.5, 2.0) were prepared via auto-combustion sol–gel method. A stoichiometric amounts of $Ba(NO_3)_2$, $Fe(NO_3)_3 \cdot 9H_2O$, $Al(NO_3)_3 \cdot 9H_2O$ and $Cr(NO_3)_3 \cdot 9H_2O$ were dissolved in deionized water and the mixture was vigorously stirred on a hotplate in 60 °C. Citric acid was weighed as a molar ratio of metal ions to citric acid of 1:5 and add into the solution. After dissolving the nitrate salts completely, the solution were allowed to cool down to room temperature and then ammoniac was added to adjust the pH value to ca. 7.0.

These solution were slowly evaporated on a hotplate at 80 °C until a highly viscous residue dried gels were formed and then the viscous residue dried gels were heated at 250 °C to ignite with the formation of large amounts of gas, resulting in light weight voluminous powder. Before annealing, the resulting precursor powders was preheated to 450 °C for 1 h to decompose the organic precursor and volatile gases. Finally, the resulting precursor powders were calcined at 950 °C for 2 h. The procedure for the synthesis of pure and substituted barium hexaferrite has been illustrated in Fig. 1.

Materials Characterization

For structural analysis, X-ray diffraction measurements were performed. A Phillip X'pert diffractometer (Model MPD-XPERT) was used carry out the experiment. A CuK_{α} beam having wavelength (λ) = 1.54 Å was used as the radiation source. The diffractometer was operated at 40 kV and 30 mA using a scanning step of 0.03 in 2θ and a dwell time of 1 s was used. The 2θ angle was varied from 10° to 100°. The FTIR spectra for all samples were characterized using a Bruker TENSOR 27 infrared spectrophotometer. The IR absorbance was measured in a range between 4000 and 400 cm^{-1}. The morphology, microstructure and chemical composition of the substituted hexaferrite nanoparticles were examined using a field emission

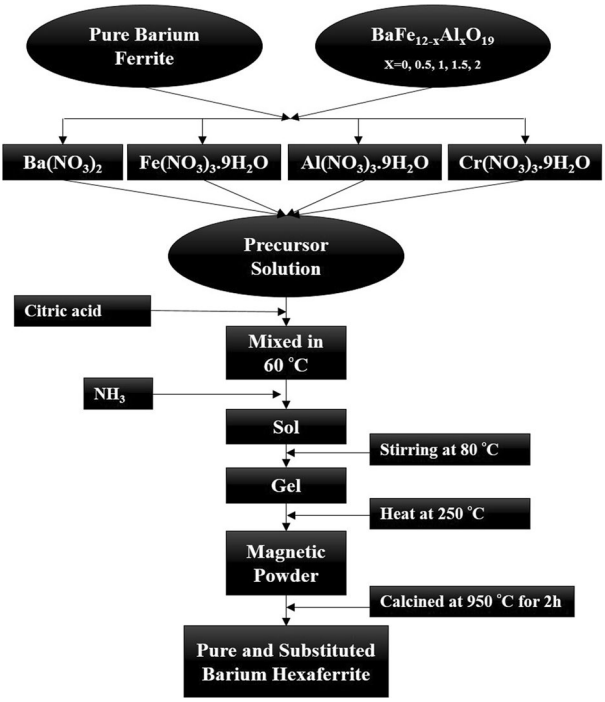

Fig. 1 The procedure for the synthesis of $BaFe_{12}O_{19}$ and $BaFe_{10.5-x}Al_{1.5}Cr_xO_{19}$

scanning electron microscope (FE-SEM; Model Mira3-XMU, TESCAN) and energy dispersive spectroscopy with 15 kV voltages, respectively. The magnetic properties of the ferrite nanoparticles such as saturation magnetization (M_s), remanence magnetization (M_r), and the coercive field (H_c) were calculated from the M–H loops, measured with a vibrating sample magnetometer (VSM; Model Kavir Magnet, Iran) in a maximum applied field of 15 kOe at room temperature.

Results and Discussion

Structural Characteristics

Figure 2 shows the X-ray diffraction patterns of pure barium ferrite and $BaFe_{10.5-x}Al_{1.5}Cr_xO_{19}$ nanoparticles with various Cr^{3+} ions contents calcined at 950 °C for 2 h. It can be seen that the positions and relative intensities of these nanoparticles peaks match well with the (110), (107), (114), (203), (205), (217) and (2011) planes and belong to the magnetoplumbite barium ferrite as revealed in the PDF. No. 01-078-0133. The powder XRD patterns of $BaFe_{12}O_{19}$ and $BaFe_{10}Al_{1.5}Cr_{0.5}O_{19}$ (x = 0.5) exhibited magnetoplumbite phase with undesired diffraction peak related to α-Fe_2O_3 phase (PDF. NO. 01-085-0599 and PDF. No. 01-084-0307, respectively). This is attributed to the incomplete reaction or blending of raw materials between Fe^{3+} and Ba^{2+} under synthesis conditions and due to the α-Fe_2O_3 is similar to $FeTiO_3$ structure which belongs to trigonal crystal structure having orthorhombic hexahedron crystal cell, it is difficult to transform the α-Fe_2O_3 into magnetoplumbite phase [9]. In the other substituted nanoparticles, this phase was not observed, but with increasing substitution of Cr^{3+} ions contents from 1.0 to 2.0, the XRD patterns of substituted nanoparticles reflect extra peaks at 27.969°, 32.288°

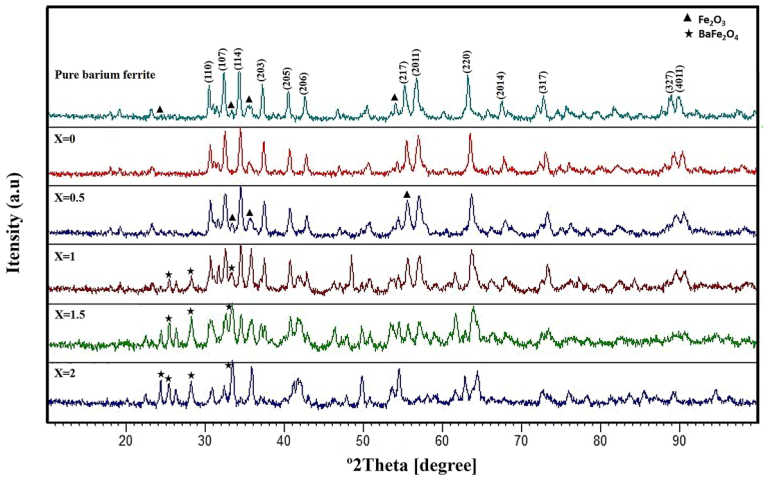

Fig. 2 XRD analysis results of pure barium ferrite and $BaFe_{10.5-x}Al_{1.5}Cr_xO_{19}$ with different Cr^{3+} ions contents (x = 0–2)

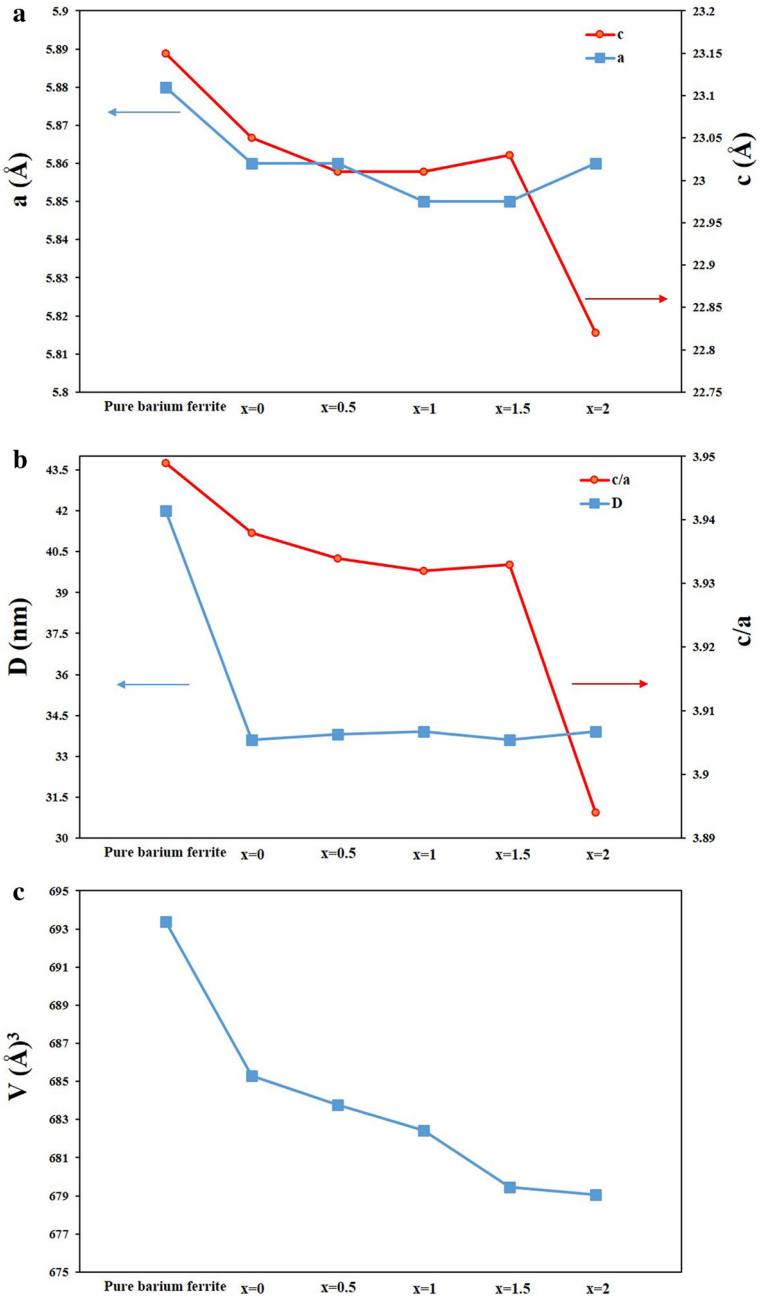

Fig. 3 Variations of microstructure characteristics (**a**) Lattice parameters (**a**, **c**), **b** the ratio of c/a and crystallite size and **c** unit cell volume of nanoparticles

and 33.137° which is the typical Bragg peaks of $BaFe_2O_4$ intermediate phase as revealed in the PDF. No. 01-077-2337. The presence of $BaFe_2O_4$ intermediate phase reflects that both the Al^{3+} and Cr^{3+} ions contents substitution leading to lack of γ-Fe_2O_3 intermediate phase which can react with $BaFe_2O_4$ phase to form the $BaFe_{12}O_{19}$ phase, hence the amount of $BaFe_2O_4$ phase to remain unreacted [4]. The complete reaction proceeds as follow:

$$BaFe_2O_4 + \gamma\text{ - }Fe_2O_3 = BaFe_{12}O_{19}$$

The lattice parameters of these nanoparticles (a and c) and unit cell volume (V_{cell}) have been calculated using the following equations [11].

$$\frac{1}{d_{hkl}^2} = \frac{4}{3}\left(\frac{h^2 + hk + k^2}{a^2}\right) + \frac{l^2}{c^2} \quad (1)$$

$$V_{cell} = 0.8666a^2c \quad (2)$$

where $d_{(hkl)}$ is the d-spacing value and (hkl) is the miller indices. Figure 3 (a and c) represents the lattice parameters and unit cell volume resulting from pure barium ferrite and substituted hexaferrite $BaFe_{10.5-x}Al_{1.5}Cr_xO_{19}$ nanoparticles. As it clear, the values of lattice parameter (c) and unit cell volume decreased with increasing the substitution contents in comparison to $BaFe_{10.5}Al_{1.5}O_{19}$ (x = 0), while the value of lattice parameter (a) remained nearly constant with the increase in Cr^{3+} ions contents. On the contrary substitution of Al^{3+} that will change both the a and c, Cr^{3+} substitution in the M-type ferrite mainly affect the c lattice parameter [5, 13]. Also, it can be seen that except $BaFe12O_{19}$ and $BaFe_{8.5}Al_{1.5}Cr_2O_{19}$ (x = 2), the contraction of crystal axis (c/a) ratio is nearly constant. These results could be due to

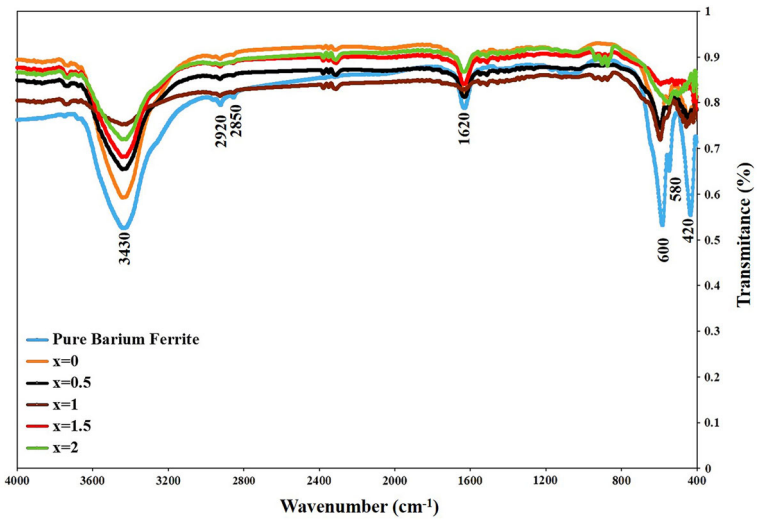

Fig. 4 FTIR spectra of the pure barium ferrite and $BaFe_{10.5-x}Al_{1.5}Cr_xO_{19}$ (x = 0–2) hexaferrite nanoparticles

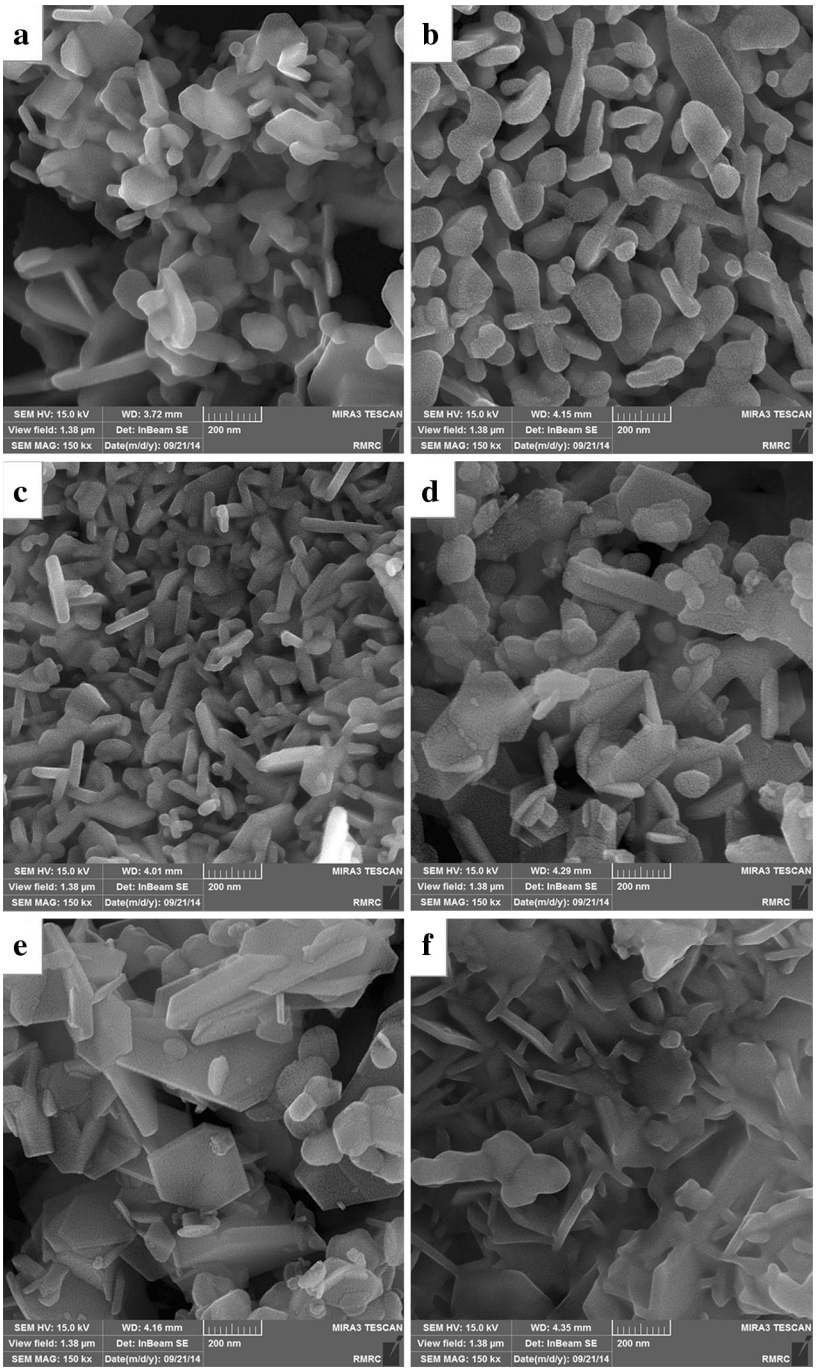

Fig. 5 Field-emission scanning electron micrographs of **a** the pure barium ferrite nanoparticles and substituted hexaferrite $BaFe_{10.5-x}Al_{1.5}Cr_xO_{19}$ nanoparticles **b** x = 0, **c** x = 0.5, **d** x = 1, **e** x = 1.5 and **f** x = 2

smaller ionic radii of substituted Al^{3+} (0.535 Å) and Cr^{3+} (0.615 Å) ions in comparison to ionic radius of Fe^{3+} ions (0.645Å). Due to the solubility of Al^{3+} and Cr^{3+} ions in the M-type hexaferrite lattice, the cell dimensions could be reduced which is in agreement with the previous literature in this field [5, 11, 12].

The Scherrer's formula was used to obtain the values of crystallite size as shown in Fig. 3b.

$$D = \frac{0.89\lambda}{\beta cos\theta} \tag{3}$$

where λ is the X-ray wavelength, β is the full-width at half max and θ is the Bragg angle [11]. As it can be seen from Fig. 3b, with substitution of Cr^{3+} ions in barium hexaferrite lattice, the crystalline size of substituted barium ferrite reduce in comparison to pure barium ferrite. In fact, when the unit cell volume reduce due to substitute Al^{3+} and Cr^{3+} ions in the lattice of $BaFe_{12}O_{19}$, during the crystal growth process, the mass transportation through adjacent crystallite is reduced and cause to a decrease in the crystallite size [14].

The investigations of chemical structure changes of a precursor powder, pure barium ferrite and the substituted hexaferrite nanoparticles were carried out by FTIR, and the FTIR spectra at the range of wave number 400–4000 cm^{-1} are shown in Fig. 4. The main features of the spectra include bands corresponding to barium hexaferrite and OH group. The bands in the range 420–450 and 540–615 cm^{-1} are corresponding to stretching vibration of metal–oxygen bond indicating the formation of hexaferrite structure including octahedral and tetrahedral sites, respectively [9, 15, 16]. On the other hand, the wavenumber being inversely proportional to the atomic weight, hence with increasing the substitution of Al^{3+} and Cr^{3+} ions contents, the peaks shift to a higher wavenumber (from 582 to 615 cm^{-1}) due to Fe^{3+} ions with a heavier atomic weight than Al^{3+} and Cr^{3+} ions and it confirms that the Al^{3+} and Cr^{3+} ions are entered to the lattice of $BaFe_{12}O_{19}$ [14]. The absorption bonds around 1623 cm^{-1} can be attributed to O–H bending band of the H_2O molecules chemically adsorbed to the magnetic particle surface. The spectra exhibit an O–H stretching mode around 3200–3500 cm^{-1} which is represented by a broad band, where freely vibrating OH groups and hydrogen bonded OH groups are apparent [15, 16]. The peaks around 2850 and 2925 cm^{-1} corresponding to the presence of C-H stretching [10].

Figure 5 shows the FE-SEM micrographs of the pure barium ferrite and substituted hexaferrite $BaFe_{10.5-x}Al_{1.5}Cr_xO_{19}$ (x = 0–2) nanoparticles with various Cr^{3+} ions contents calcined at 950 °C for 2 h. As it can be seen, in all of the samples, the nanoparticles have been distributed homogeneously and closely packed throughout the surface of sample and the hexagonal structure is clear. As shown in Fig. 6, with substituting Cr^{3+} ions in the hexagonal structure of barium ferrite the mean particle size of $BaFe_{10.5-x}Al_{1.5}Cr_xO_{19}$ (x = 0–2) along c-axis are less than 55 nm and reduced in comparison to $BaFe_{12}O_{19}$. It can be attributed to the presence of Al^{3+} and Cr^{3+} ions on the grain boundaries which lead to hindering of growth in some of the crystallographic planes and encouraging of growth in other directions. On the other hand, with increasing substitution of Cr^{3+} ions, the morphology of

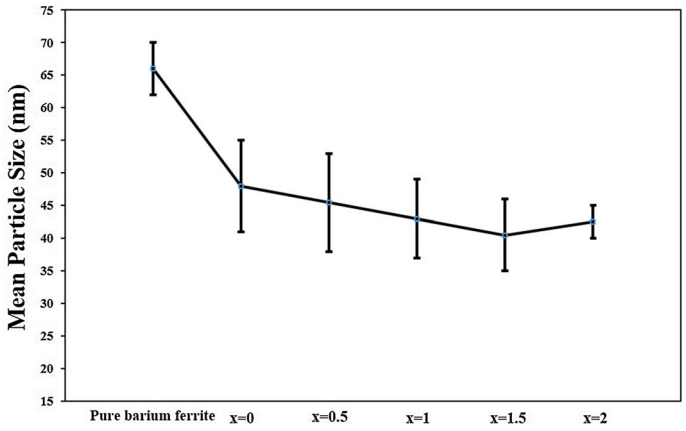

Fig. 6 Mean particle size of the $BaFe_{12}O_{19}$ and substituted $BaFe_{10.5-x}Al_{1.5}Cr_xO_{19}$ hexaferrite with different Cr^{3+} ions contents

nanoparticles are turning from nanospherical shape (equiaxed morphology) to nanodisk and nanorods (35–70 nm).

The elemental analysis were carried out by the energy-dispersive spectroscopy (EDS) to confirm the chemical composition of the substituted hexaferrite nanoparticles and the corresponding results are presented in Table 1. It is evident from the elemental analysis that the atomic percentage (at.%) of Ba, Fe, Al and Cr in the $BaFe_{10.5-x}Al_{1.5}Cr_xO_{19}$ nanoparticles basically agree with the designed composition and the stoichiometric Cr^{3+} ions substitution contents were increased while the Fe^{3+} ions contents decreased. Figure 7 shows the typical EDS spectra of the pure barium ferrite and substituted hexaferrite nanoparticles.

Magnetic Properties

The magnetic properties of the $BaFe_{12}O_{19}$ and substituted hexaferrite $BaFe_{10.5-x}Al_{1.5}Cr_xO_{19}$ nanoparticles with different Cr^{3+} ions contents were measured at a maximum applied of 15 kOe at room temperature. The typical hysteresis loops (M-H curves) of the nanoparticles are plotted in Fig. 8 and the magnetic parameters are presented in Table 2. The amount of substituting has a significantly influence on

Table 1 Energy dispersive X-ray analysis results of $BaFe_{12}O_{19}$ and $BaFe_{10.5-x}Al_{1.5}Cr_xO_{19}$ nanoparticles

X	Elemental compositions (wt %)			
	Ba	Fe	Al	Cr
Pure barium ferrite	13.69	34.23	0.0	0.0
x = 0	11.86	51.34	2.04	0.0
x = 0.5	12.42	50.67	3.03	1.98
x = 1	12.51	44.34	3.72	3.99
x = 1.5	13.13	42.93	3.61	6.21
x = 2	13.72	36.24	3.63	8.57

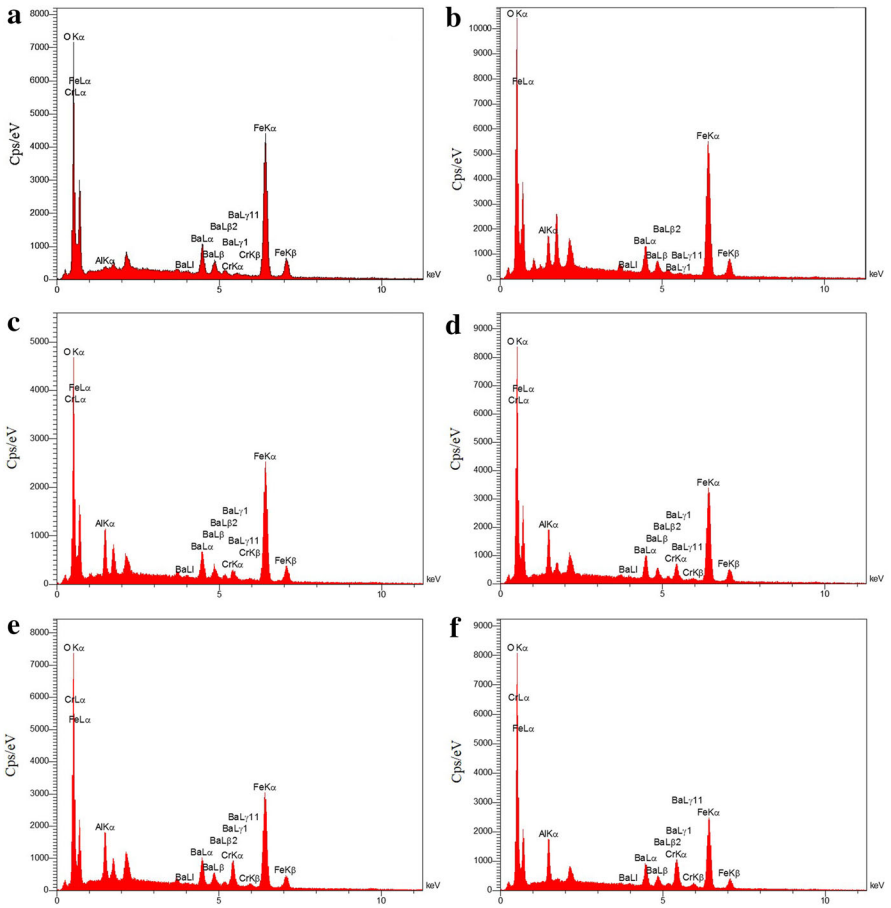

Fig. 7 The typical EDS spectra of **a** the $BaFe_{12}O_{19}$ and substituted hexaferrite $BaFe_{10.5-x}Al_{1.5}Cr_xO_{19}$ nanoparticles **b** x = 0, **c** x = 0.5, **d** x = 1, **e** x = 1.5 and **f** x = 2

magnetic properties. As it can be observed in Fig. 9, in comparison to pure barium ferrite, the saturation magnetization (M_s) and remanence magnetization (M_r) is decreased, but the coercive field (H_c) did not have any specific trend with an increase in the amount of Cr^{3+} ions substitution in the composition. The decrease in M_s and M_r with chemical composition can be justified based on the different sites that occupied by substituted Al^{3+} and Cr^{3+} ions on the structure of barium hexagonal ferrite. The Al^{3+} (0 μ_B) and Cr^{3+} (3 μ_B) ions are mainly substituted Fe^{3+} (5 μ_B) ions in 12 k sites (upward spin) and lead to a reduction in M_s and M_r synthesized nanoparticles. On the other hand, small amounts of chromium substitution can be increased in saturation magnetization due to the number of substituted Cr^{3+} ions in $4f_2$ sites (downward spin) is more than 12 k and 2b sites (upward spin). It could be the reason for the higher saturation magnetization of small substituted Cr^{3+} nanoparticles (x = 0.5) in comparison to other substituted

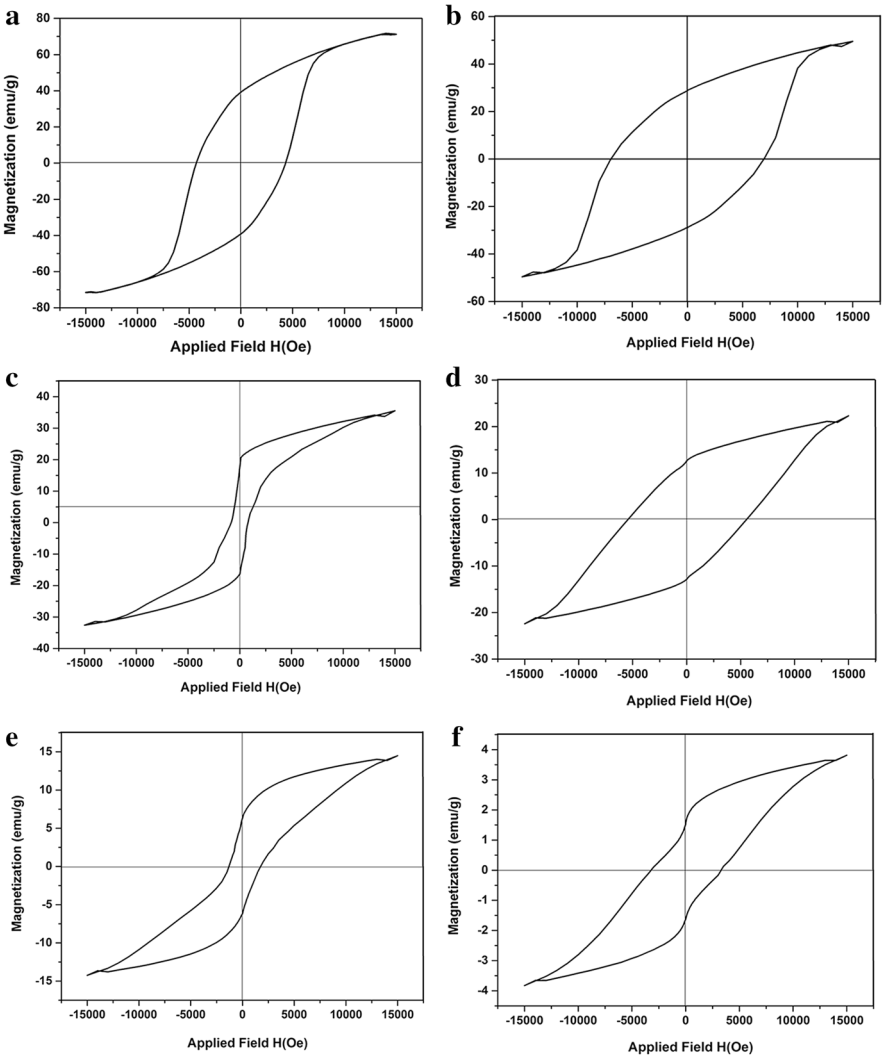

Fig. 8 The typical hysteresis loops of the as-synthesized **a** pure barium ferrite nanoparticles and substituted $BaFe_{10.5-x}Al_{1.5}Cr_xO_{19}$ nanoparticles **b** x = 0, **c** x = 0.5, **d** x = 1, **e** x = 1.5 and **f** x = 2

Cr^{3+}nanoparticles. Also, the substitution of Fe^{3+} ions by Al^{3+} and Cr^{3+} ions lead to reduce superexchange interaction between Fe^{3+}-O-Fe^{3+} and it may be caused to a non-collinear spin arrangement (spin canting) [5, 11, 12]. Moreover, the presence of impurity like α-Fe_2O_3 (in pure barium ferrite and $BaFe_{10}Al_{1.5}Cr_{0.5}O_{19}$) and $BaFe_2O_4$ ($x > 0.5$) have a significant influence on decrease in M_s and M_r. It is possible to reduce the particle size lower than single domain critical size, hence the nanoparticles show paramagnetic behavior with increasing the substitution of Cr^{3+}

Table 2 Magnetic properties of pure barium ferrite and substituted $BaFe_{10.5-x}Al_{1.5}Cr_xO_{19}$ nanoparticles

X	M_s (emu/g)	M_r (emu/g)	H_c (Oe)
Pure barium ferrite	71	39	4450
x = 0	50	29	6933
x = 0.5	36	16	833
x = 1	22	13	5558
x = 1.5	15	6	1393
x = 2	3.85	1.56	3196

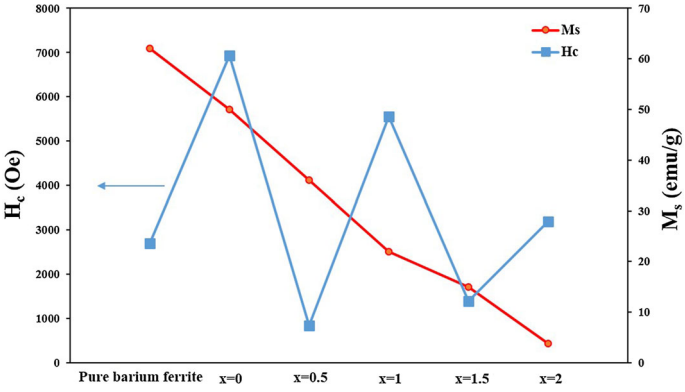

Fig. 9 The saturation magnetization (M_s) and coercive field (H_c) of pure barium ferrite and substituted $BaFe_{10.5-x}Al_{1.5}Cr_xO_{19}$ hexaferrite with different Cr^{3+} ions contents (x = 0–2)

ions in the crystal structure of barium ferrite, as well as substituting Al^{3+} ions. Therefore the saturation magnetization and remanence magnetization are reduced.

It is observed from Fig. 9 and Table 2, the H_c values of Cr^{3+} substituted barium hexaferrite did not have any specific trend and the $BaFe_{10.5}Al_{1.5}O_{19}$ (x = 0) nanoparticle shows the highest coercivity field (6933 Oe) in comparison to pure barium ferrite and other substituted nanoparticles. The coercive field is strongly dependent on particle size and magnetocrystalline anisotropy. As concluded from FE-SEM data (Figs. 5, 6), the mean particle size of substituted barium ferrite (about 50 nm) was lower than critical diameter of the spherical M-type hexaferrite with single magnetic domain, hence all of substituted nanoparticle consist of single magnetic domains and they can act as a barrier to the movement of the domain walls, which leading to an increase in the H_c. But the H_c values have been decreased in $BaFe_{10}Al_{1.5}Cr_{0.5}O_{19}$ (x = 0.5) and $BaFe_9Al_{1.5}Cr_{1.5}O19$ (x = 1.5) in comparison to pure barium ferrite. It can be attributed to simultaneous substitution of $Al^{3+}$and Cr^{3+} ions in the structure of barium hexaferrite which leading to a decrease in particle size of nanoparticles lower than superparamagnetic area, so the hysteresis loops of nanoparticle with x = 0.5 and x = 1.5 have a mixture of ferrimagnetic and paramagnetic component of the sample [5, 17].

As it is well known, in according to $H_c = 2K_1/M_s$ (where H_c is the coercive field, K_1 is anisotropic constant and M_s is saturation magnetization), H_c and M_s are inversely proportional [4, 10]. However, as it can be observed from Table 2, the H_c values not be increased with decreasing M_s at Cr^{3+} substituted nanoparticles (except at x = 1). This result could be explained by reduction in magnetocrystalline anisotropy. Concerning the magnetic anisotropy, the Al^{3+} ions can occupied 2a, $4f_1$, $4f_2$ and 12 k sites, so it has no significant effect on magnetocrystalline anisotropy, while the M_s values of substituted hexaferrite have been dramatically decreased [5]. On the other hand, there is strong competition between Cr cations and Al cations for substituting at these sites. Therefore, when one cation substituted at these sites (e.g. Al), another cation (e.g. Cr) may be substituted at the other sites (that have a significant effect on magnetocrystalline anisotropy), which lead to decrease in magnetocrystalline anisotropy and consequently decrease in H_c.

Another factor that plays a role in the magnetocrystalline anisotropy changes, is 2b site in the crystal structure of M-type ferrites. The Al^{3+} ions (in small substitution, x = 1.5) are not replaced Fe^{3+} ions at trigonal bipyramidal 2b sites, thus it has a very little effect on the magnetiocrystalline anisotropy [5, 18, 19]. However, due to the presence of Cr^{3+} ions in addition to Al^{3+} ions in chemical composition, Cr^{3+} ions can occupy sites in the lattice that could already be occupied by Al^{3+} ions, thereby the Al^{3+} ions may be occupied 2b sites and lead to decrease in magnetiocrystalline anisotropy and coercive field. The ratio of c/a is also another factor that affected on coercive field. It can be seen from Fig. 3b that the ratio of c/a decrease with increasing substitution of Cr^{3+} ions due to the value of lattice parameter (c) decreased and the value of lattice parameter (a) remained nearly constant. This can reduce the H_c values in the rotation magnetization process [13].

Conclusion

Pure barium ferrite and substituted Cr^{3+} nanoparticles of $BaFe_{10.5-x}Al_{1.5}Cr_xO_{19}$ (x = 0–2) have been successfully fabricated via auto-combustion sol–gel method. It was revealed from XRD patterns and FE-SEM micrographs that in all of nanoparticles the hexagonal phase has been formed and the value of lattice parameter (c) decreased, while the value of lattice parameter (a) remained nearly constant with the increase in Cr^{3+} ions contents. The crystallite size and mean particle size of the nanoparticles lie in the ranges 33–42 and 35–70 nm, respectively. The formation of hexaferrite structure including octahedral and tetrahedral sites was confirmed by FTIR. The saturation magnetization (M_s) has been dramatically decreased from 71 to 3.85 emu/g due to the reduction of the superexchange interaction between Fe^{3+}-O-Fe^{3+} and the non-collinear spin arrangement magnetic moment, while coercive field (H_c) increased from 4.45 kOe for pure barium ferrite to 6.9 kOe for $BaFe_{10.5}Al_{1.5}O_{19}$ (x = 0). The enhancement in coercivity field may be explained on the basis of the increase in the magnetocrystalline anisotropy and the decrease of the particle size. In the others substitution of Cr^{3+} ions, the H_c values decreased in comparison to $BaFe_{10.5}Al_{1.5}O_{19}$.

References

1. R. C. Pullar (2012). *Prog. Mater. Sci.* **57**, 1191.
2. M. V. Kuznetsov, L. F. Barquín, Q. A. Pankhurst, and I. P. Parkin (1999). *J. Phys. D* **32**, 2590.
3. A. Kaewrawang, A. Ghasemi, X. Liu, and A. Morisako (2009). *J. Magn. Magn. Mater.* **321**, 1939.
4. C. Li, B. Huang, and J. Wang (2013). *J. Mater. Sci.* **48**, 1702.
5. H. Luo, B. K. Rai, S. R. Mishra, V. V. Nguyen, and J. P. Liu (2012). *J. Magn. Magn. Mater.* **324**, 2602.
6. A. Hojjati Najafabadi, R. Mozaffarinia, and A. Ghasemi (2015). *J. Supercond. Nov. Magn.* **28**, 2821.
7. B. K. Rai, S. R. Mishra, V. V. Nguyen, and J. P. Liu (2013). *J. Alloys Compd.* **550**, 198.
8. J. Luo (2012). *Mater. Lett.* **80**, 162.
9. A. Thakur, R. R. Singh, and P. B. Barman (2013). *Mater. Chem. Phys.* **141**, 562.
10. M. Asghari, A. Ghasemi, E. Paimozd, and A. Morisako (2013). *Mater. Chem. Phys.* **143**, 161.
11. I. Ali, M. U. Islam, M. S. Awan, and M. Ahmad (2013). *J. Alloys Compd.* **547**, 118.
12. S. Ounnunkad, P. Winotai, and J. Magn (2006). *Magn. Mater.* **301**, 292.
13. Q. Fang, H. Cheng, K. Huang, J. Wang, R. Li, and Y. Jiao (2005). *J. Magn. Magn. Mater.* **294**, 281.
14. M. Liu, X. Shen, F. Song, J. Xiang, and X. Meng (2011). *J. Solid State Chem.* **184**, 871.
15. F. Khademi, A. Poorbafrani, P. Kameli, and H. Salamati (2012). *J. Supercond. Nov. Magn.* **25**, 525.
16. A. Thakur, R. R. Singh, and P. B. Barman (2013). *J. Magn. Magn. Mater.* **326**, 35.
17. A. Roberts, Y. Cui, and K. L. Verosub (1995). *J. Geophys. Res.* **100**, 17909.
18. Y. Xu, G. L. Yang, D. P. Chu, and H. R. Zhai (1990). *J. Physica Status Solidi B* **157**, 685.
19. G. Albanese, M. Carbucicchio, and A. Deriu (1973). *J. II Nuovo Cimento B* **15**, 17.